

# **Ambient Conversion of Carbon Dioxide into Liquid Fuel by a Heterogeneous Synergetic Dual Single-Atom Catalyst**

Guoqing Ren <sup>a,†</sup>, Jikai Sun <sup>a,†</sup>, Shengliang Zhai <sup>a</sup>, Li Yang <sup>a</sup>, Tie Yu <sup>a</sup>, Lei Sun <sup>a,\*</sup>, and  
Weiqiao Deng <sup>a,b,\*</sup>

<sup>a</sup> *Institute of Molecular Sciences and Engineering, Institute of Frontier and Interdisciplinary Science, Shandong University, Qingdao, Shandong, 266237, P. R. China.*

<sup>b</sup> *State Key Laboratory of Molecular Reaction Dynamics, Dalian Institute of Chemical Physics, Dalian, 116023, P. R. China.*

<sup>†</sup> *These authors contributed equally.*

\* Corresponding author

Lei Sun: slei@sdu.edu.cn, Weiqiao Deng: dengwq@sdu.edu.cn

**Abstract:**

Ambient conversion of carbon dioxide into various liquid fuels or chemicals is a potential economical solution for reducing CO<sub>2</sub> emissions, which may be responsible for recent climate change. Here, we report a highly active dual single-Pd-atom catalyst for ambient conversion of CO<sub>2</sub> to formic acid using a step-by-step catalyst design strategy by the density functional theory (DFT) method. The theoretically predicted catalyst is synthesized experimentally and verified to capture a significant amount of CO<sub>2</sub> (5.05 mmol/g, 273 K), and it can efficiently convert CO<sub>2</sub> to formic acid under ambient conditions (30 °C, 1 bar) with a turnover frequency (TOF) as high as 13.46 h<sup>-1</sup>, which is the first such report in the field of heterogeneous catalysts. Two major factors contributing to this extraordinary catalytic activity include a pore enrichment effect of the microporous structures of the covalent triazine framework and a ternary synergetic effect among two neighbouring Pd atoms and rich nitrogen environment. Our work may aid the development of heterogeneous catalysts to produce other commonly used fuels from CO<sub>2</sub> under ambient conditions.

## Main

With the unrestrained use of fossil energy, excessive emission of CO<sub>2</sub> has become one of the most concerning environmental problems in the world. The selective hydrogenation of CO<sub>2</sub> into useful liquid fuels is regarded as the most promising route to replace fossil feedstocks and realize CO<sub>2</sub> emission reduction.<sup>1, 2, 3</sup> Hydrogenation of CO<sub>2</sub> to formic acid, one of the most basic liquid fuels, which is present as formate in practical production to shift thermodynamic equilibrium forward, has attracted increasing attention in recent years.<sup>4, 5, 6</sup> Moreover, with the rapid development of formic acid dehydrogenation techniques, formic acid is expected to become an attractive hydrogen carrier in fuel cells with its great advantages of high volumetric hydrogen density (53 g H<sub>2</sub> per litre of HCOOH), high chemical stability, and low toxicity.<sup>6, 7, 8</sup> Thus, developing an efficient catalyst system for CO<sub>2</sub> capture and conversion to formate without further energy input (ambient conversion) is highly desired and could result in a truly carbon-neutral liquid fuel.

Great efforts have been made to conduct CO<sub>2</sub> conversion to formate, including the use of homogenous organometallic complexes<sup>9, 10, 11</sup>, immobilized organometallic complexes<sup>12, 13</sup> and supported noble metal nanoparticles<sup>14, 15, 16</sup>. Among them, homogeneous catalyst systems can achieve the target of ambient conversion of gaseous CO<sub>2</sub>. For example, Fujita, Himeda *et al.*<sup>17, 18, 19, 20, 21</sup> reported a series of half-sandwich Ir(III) complexes, which realized the formation of formate from CO<sub>2</sub> at 25 °C and 1 bar by modulating the electron donating effect of the ligands. Linehan *et al.*<sup>22</sup> reported a noble-metal free molecular catalyst system for the production of formate from CO<sub>2</sub> and H<sub>2</sub> at room temperature and atmospheric pressure. However, the disadvantages of homogeneous catalytic systems, such as poor reaction continuity, poor stability, and difficulty in product separation, prevent their large-scale application. It is of great significance to develop a heterogeneous catalytic system for the conversion of gaseous CO<sub>2</sub> to formic acid under ambient conditions, which hasn't been reported in the literature. Single-atom catalysts (SACs),<sup>23, 24, 25, 26</sup> a new frontier in heterogeneous catalysis, which have advantages of both homogeneous and

heterogeneous catalysts, are expected to be potential catalysts for the hydrogenation of CO<sub>2</sub> to formic acid under ambient conditions. Shao *et al.*<sup>27</sup> demonstrated that SACs are highly effective for the hydrogenation of CO<sub>2</sub> to formic acid by constructing an atomically dispersed Ir catalyst, which presented the best performance to date for heterogeneous conversion of CO<sub>2</sub> to formate under high temperature and pressure conditions. Unfortunately, even SACs cannot achieve ambient conversion of CO<sub>2</sub> to formic acid. Compared to SACs, dual single-atom catalysts with synergistic effects between adjacent metal atoms and tuneable electronic environments could further improve the intrinsic activity of the catalyst.<sup>28, 29, 30, 31, 32</sup> However, these researches on CO<sub>2</sub> hydrogenation mainly focus on electrocatalysis<sup>32, 33, 34</sup> or high temperature and high pressure operation conditions<sup>31</sup>. Therefore, rational design of highly efficient dual single-atom catalysts with multi- synergetic sites may realize ambient conversion of CO<sub>2</sub> to formic acid.

In this work, we realized ambient conversion of CO<sub>2</sub> to formic acid by a heterogeneous catalyst, which consists of dual Pd single atoms anchoring on a microporous layered 2,6-pyridinedicarbonitrile-derived covalent triazine framework (*2,6-DCP-CTF*). First, we screened seven noble metal SACs by using the DFT method and predicted Pd as the most active metal for the hydrogenation of CO<sub>2</sub> to formic acid among various noble metals. Furthermore, we found that the dual Pd atoms within nitrogen rich environment exhibited a much lower barrier for this reaction than that of the Pd single atom, indicating that a ternary synergetic effect among two neighbouring Pd atoms and rich nitrogen environment could further improve the intrinsic activity of Pd. The experimental results verified the predictions. By regulating the loading percentage of Pd, we obtained Pd/[*2,6-DCP-CTF*] with abundant dual Pd atoms, which achieved ambient conversion of CO<sub>2</sub> to formic acid. As a typical example of a theoretical prediction experiment, this work is expected to play an important role in the design of CO<sub>2</sub> conversion catalysts at room temperature and atmospheric pressure in the future.

## **Results and discussion**

## Theoretical screening of noble metal SACs

To save effort, we first carried out theoretical screening of noble metal SACs for the proof of concept. To simplify, 1,3,5-triazine,2-(2-pyridinyl) ligand-anchored single noble metal atoms were used as SAC models for CO<sub>2</sub> hydrogenation. It was previously reported that the first hydrogenation step is the rate-determining step for CO<sub>2</sub> hydrogenation to formate.<sup>12, 35</sup> Thus, we chose the first hydrogenation step of CO<sub>2</sub> to formate as the criterion to explore the most active sites for CO<sub>2</sub> activation among seven different noble metal ions (Ru, Rh, Pd, Ir, Pt, Au, and Os) by using DFT method. We compared the adsorption energies of CO<sub>2</sub> on the above noble metal atoms and their corresponding ions. It was found that the absolute values of the adsorption energies on the metal atoms were much lower than those on their corresponding ions (Supplementary Fig. 1). Taking the adsorption configuration of Pd-based catalysts as an example, CO<sub>2</sub> is physically adsorbed on 2,6-DCP-CTF-[Pd<sup>0</sup>] with a Pd-O bond length of 3.1 Å, while its adsorption on 2,6-DCP-CTF-[Pd<sup>2+</sup>] is stronger with a Pd-O bond length of 2.2 Å (Supplementary Fig. 2). Therefore, the above seven kinds of noble metal ions dispersed on 2,6-DCP-CTF were adopted as active sites for CO<sub>2</sub> hydrogenation. The computational results of the energy barriers of the first hydrogenation step of CO<sub>2</sub> to formate on 2,6-DCP-CTF-[M<sup>δ+</sup>] are shown in Fig. 1a and Supplementary Table 1. Fig. 1a shows that 2,6-DCP-CTF-[Pd<sup>2+</sup>] presents the lowest energy barrier of 1.37 eV, which indicates that Pd is the most effective metal for CO<sub>2</sub> activation among the seven noble metals assessed.

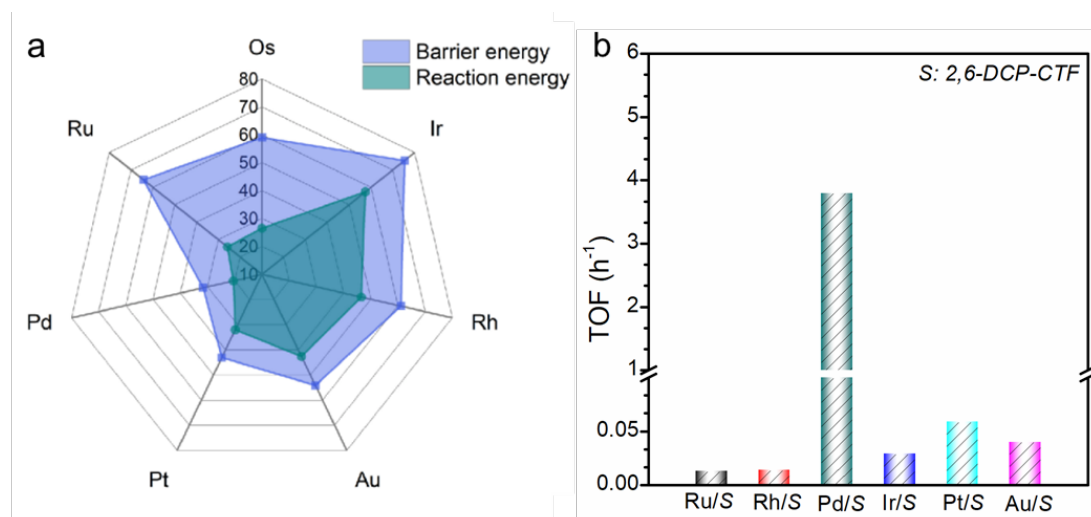


**Fig. 1** Theoretical screening of noble metal SACs (a) and their corresponding catalytic activity for CO<sub>2</sub> hydrogenation to formate in experiment (b). Reaction conditions: 20 mg catalyst, 5 ml of 1 M NaHCO<sub>3</sub> solvent, 30 °C, 0.1 MPa, and 12 h.

Then, we chose six of the most commonly used noble metals (Ru, Rh, Pd, Ir, Pt, Au) as examples to confirm the above theoretical predictions. *2,6-DCP-CTF* was prepared by the traditional ionothermal method by trimerization of *2,6-DCP* in molten ZnCl<sub>2</sub> at 400 °C for 20 h and 600 °C for another 20 h (Fig. 2a).<sup>36</sup> The formation of the corresponding covalent triazine rings was confirmed by Fourier transform infrared spectroscopy (FT-IR). As shown in Fig. 2b, *2,6-DCP* possesses a clear cyano group absorption peak at 2245 cm<sup>-1</sup>. This peak disappeared completely after the formation of *2,6-DCP-CTF*, and the characteristic absorption peaks of the triazine ring at 1540 cm<sup>-1</sup> and 1100 cm<sup>-1</sup> were visible, which indicated that the trimerization was complete. In addition, the porosity and elemental contents of *2,6-DCP-CTF* were determined. Specifically, the prepared *2,6-DCP-CTF* exhibits adsorption properties typical of microporous materials and has a specific surface area of 1964 m<sup>2</sup>/g, three types of pores with sizes of 0.57, 1.4, and 2.7 nm and a total pore volume of 1.54 cm<sup>3</sup>/g (Fig. 2c, Supplementary Table 2). The nitrogen content was estimated to be 8.01 wt.% (Supplementary Table 3), which is lower than the theoretical value (32.6%). This suggests that the material generates a considerable number of voids or defect sites during the trimerization process at high temperature. The morphological characteristics of *2,6-DCP-CTF* were detected by using scanning electron microscopy

(SEM) and transmission electron microscopy (TEM). As shown in Fig. 2d and Supplementary Fig. 3, *2,6-DCP-CTF* exhibited obvious layered properties, which is consistent with the schematic model in Fig. 2a.  $M[2,6-DCP-CTF]$  ( $M = \text{Ru}, \text{Rh}, \text{Pd}, \text{Ir}, \text{Pt}, \text{Au}$ ) catalysts were prepared by soaking the support powders into the corresponding aqueous noble metal salt solutions with a 1 wt.% theoretical loading percentage followed by filtration, washing, and drying after stirring for 12 h under a  $\text{N}_2$  atmosphere.

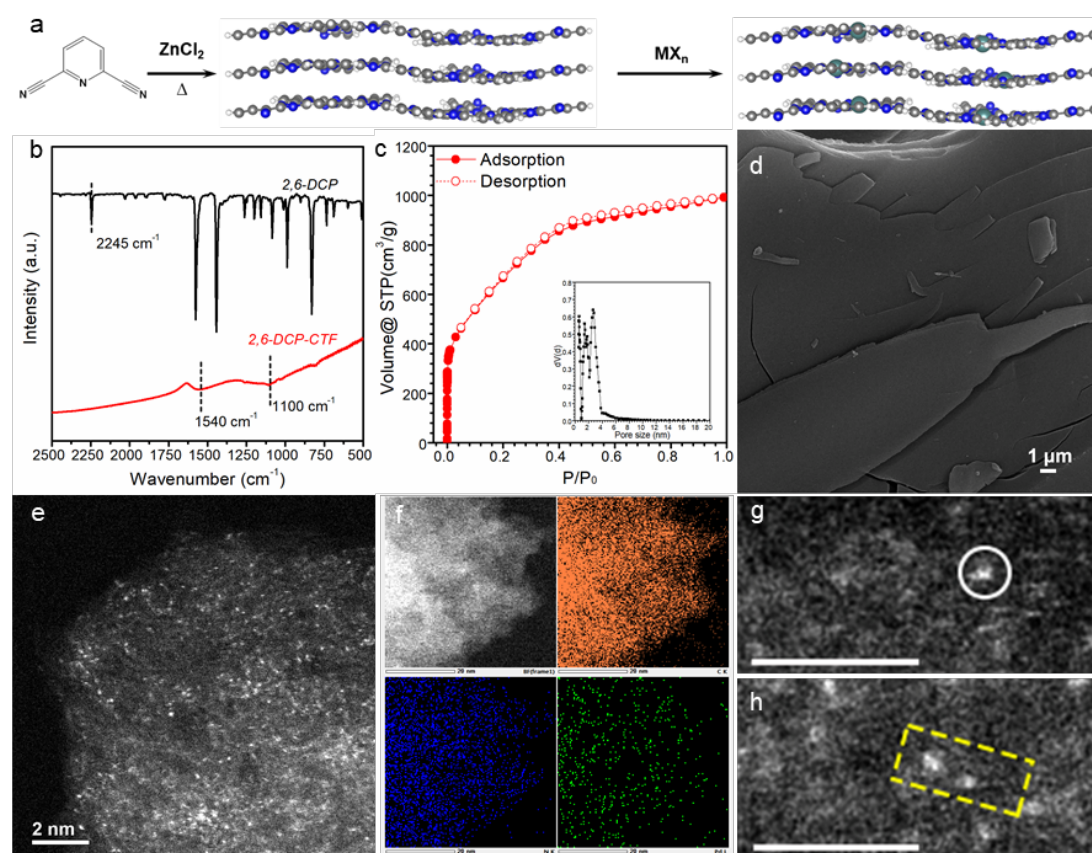


**Fig. 2** Synthesis and structural characterizations of *2,6-DCP-CTF* and  $\text{Pd}/[2,6-DCP-CTF]$ . a, Schematic illustration of the fabrication procedure of the *2,6-DCP-CTF* and  $M[2,6-DCP-CTF]$  catalysts. b, FT-IR spectra of the monomer *2,6-DCP* and *2,6-DCP-CTF* samples. c,  $\text{N}_2$  adsorption-desorption isotherms (77 K) and DFT method pore size distribution of *2,6-DCP-CTF*. d, SEM images of *2,6-DCP-CTF*. e, Aberration-corrected STEM of  $\text{Pd}/[2,6-DCP-CTF]$ . f, EDS mapping results of  $\text{Pd}/[2,6-DCP-CTF]$ . g, h, Magnified HAADF-STEM image of  $\text{Pd}/[2,6-DCP-CTF]$  (the scale bar is 1 nm).

The catalytic performances of the as-prepared  $M/[2,6\text{-DCP-CTF}]$  catalysts for  $\text{CO}_2$  hydrogenation were studied at  $30\text{ }^\circ\text{C}$  in a  $\text{H}_2/\text{CO}_2$  mixture (0.1 MPa) with  $\text{NaHCO}_3$  (1 M) as an additive in the liquid phase. After reaction for 12 h, formate was detected using high-performance liquid chromatography (HPLC). As shown in Fig. 1b and Supplementary Table 4,  $\text{Pd}/[2,6\text{-DCP-CTF}]$  exhibited the highest turnover frequency of  $3.80\text{ h}^{-1}$  among the six catalysts, which confirmed the predictions of the theoretical calculations. The catalytic activities of the six catalysts are in the order of  $\text{Pd}/[2,6\text{-DCP-CTF}] > \text{Pt}/[2,6\text{-DCP-CTF}] > \text{Au}/[2,6\text{-DCP-CTF}] > \text{Ir}/[2,6\text{-DCP-CTF}] > \text{Rh}/[2,6\text{-DCP-CTF}] > \text{Ru}/[2,6\text{-DCP-CTF}]$ . The above experiments verified the theoretical predictions that Pd is the most effective metal for the hydrogenation of  $\text{CO}_2$  to formate. Based on the  $\text{Pd}/[2,6\text{-DCP-CTF}]$  catalyst, we explored the fine structure of Pd by using aberration-corrected STEM. As shown in Fig. 2e, Pd exhibited atomic dispersion on the support, and the white dots were identified as Pd species according to the contrast and EDS mapping analysis (Fig. 2f, Supplementary Fig. 4). In addition, there were two kinds of Pd species in the observation range: single- and dual-Pd-atom species (Figs. 2g and 2h).

### **Optimization of the $\text{Pd}/[2,6\text{-DCP-CTF}]$ structure and performance**

To distinguish which Pd species contribute to the hydrogenation of  $\text{CO}_2$  into formic acid, we carried out theoretical calculations. Based on the experimental results, we rebuilt the theoretical model. As shown in Fig. 3a,  $2,6\text{-DCP-CTF}$ , possessing a two-dimensional structure, consists of two types of pores. The initial periodic structure contains abundant nitrogen atoms with a weight loading of 32.6%. Under the ionothermal process at high temperature ( $600\text{ }^\circ\text{C}$ ) in the experiment, carbonation of the sample occurs. Most of the nitrogen atoms would be replaced by carbon atoms, leading to a low nitrogen weight loading of 8.01%. In addition, structural collapse makes many larger pores. Through-pores (in Fig. 3b) with enough nitrogen atoms in the framework structure of  $2,6\text{-DCP-CTF}$  were necessary to anchor neighbouring Pd atoms in the framework. Moreover, we investigated the  $\text{CO}_2$  uptake performance. As shown in Fig. 3c, the nitrogen-rich pores, which are good  $\text{CO}_2$  adsorbents, have a high

CO<sub>2</sub> concentration at 303 K. The pore-enrichment effect favours CO<sub>2</sub> conversion and can increase the reaction rate.<sup>37,38</sup>

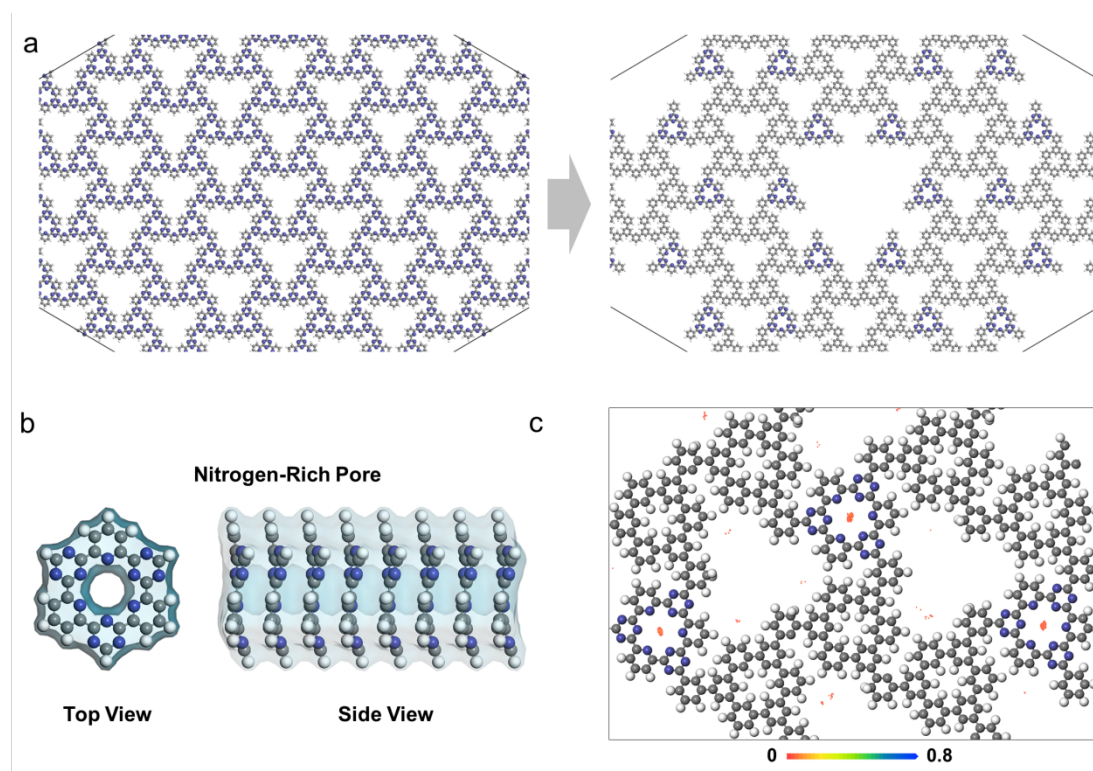


**Fig. 3. Framework structure of 2,6-DCP-CTF.** a. Schematic of structural changes before and after ionothermal processing at high temperature (600 °C). b. Schematic of a nitrogen-rich pore. c. CO<sub>2</sub> density map in the final framework structure of 2,6-DCP-CTF.

Based on the above understandings, the Pd/[2,6-DCP-CTF] dual single-atom model was built to evaluate the free energy barrier of CO<sub>2</sub> hydrogenation, in which two Pd<sup>2+</sup> ions were anchored in the neighbouring layers through the Pd-N coordination bonds (Supplementary Fig. 5). Hydrogen dissociation was first investigated. As shown in Fig. 4a, the hydrogen molecule was easily dissociated with the help of the N atoms in the paratriazine ring. The free energy barrier of hydrogen dissociation was only 2.78 kcal/mol. The synergetic effect between Pd and N contributes to hydrogen dissociation under ambient conditions, providing abundant active hydrogen to further reaction. Two reaction pathways for CO<sub>2</sub> hydrogenation on Pd/[2,6-DCP-CTF] are shown in Figs. 4b and 4c. The pathway starting from the

configuration of hydrogen and CO<sub>2</sub> co-adsorbed on a single Pd atom is the Pd<sub>1</sub> pathway. For the Pd<sub>2</sub> pathway, CO<sub>2</sub> is adsorbed on one Pd atom, while hydrogen is adsorbed on another Pd atom. The intermediate structures of CO<sub>2</sub> adsorption and hydrogenation in the Pd<sub>1</sub> system and Pd<sub>2</sub> system are shown in Fig. 4c. The adsorption energies of hydrogen and CO<sub>2</sub> in these two systems are similar. However, there is an obvious energy barrier difference between the two reaction pathways. The free barrier energy in the Pd<sub>1</sub> pathway is 34.1 kcal/mol, while that in the Pd<sub>2</sub> pathway is 21.7 kcal/mol. The synergy of the neighbouring Pd<sup>2+</sup> ions improved the activity of CO<sub>2</sub> hydrogenation in the Pd<sub>2</sub> pathway. In addition, we further calculated the reaction path of formate radical hydrogenation to formic acid. As shown in Supplementary Fig. 6, there are also two pathways for formate radical hydrogenation. The free energy barriers of these two paths are 2.2 kcal/mol and 9.1 kcal/mol, respectively. Thus, the rate-determining step of hydrogenation of CO<sub>2</sub> to formic acid is indeed the step of CO<sub>2</sub> hydrogenation.

Furthermore, we studied the mechanism of the high activity of the dual-atom system at the microscopic electron level. As shown in Fig. 4c, in the Pd<sub>1</sub> pathway, the adsorbed CO<sub>2</sub> and H in the initial state (IS) are far away, and the C-H bond length is 3.43 Å. While in the Pd<sub>2</sub> pathway, the C-H bond length is 2.60 Å. The interaction region indicator (IRI)<sup>39, 40</sup> for the co-adsorption configurations of CO<sub>2</sub> and H in the two pathways were analysed. As shown in Fig. 4d, in the Pd<sub>2</sub> system, there is a vdW interaction between adsorbed H and CO<sub>2</sub>. Thus, the H is easier to transfer to CO<sub>2</sub>. Besides, the atom charges of H in the Pd<sub>1</sub> and Pd<sub>2</sub> pathways are 0.29 e and 0.15 e. In comparison, the atom charges of C atoms of CO<sub>2</sub> in both pathways are 0.87 e. Thus, H with a low charge is more easily transfer to the C atom of CO<sub>2</sub>. Moreover, in addition to the bonding interaction between H and its adsorbing Pd<sup>2+</sup> (Pd-I), the H atom was also attracted by the Pd<sup>2+</sup> ion (Pd-II) in the neighbouring layer. The attraction of Pd-II to H weakens the adsorption interaction between H and Pd-I, which favours H to leave Pd and transfer to CO<sub>2</sub>. Therefore, the dual-atom system shows better catalytic activity for the hydrogenation of CO<sub>2</sub> to formic acid.

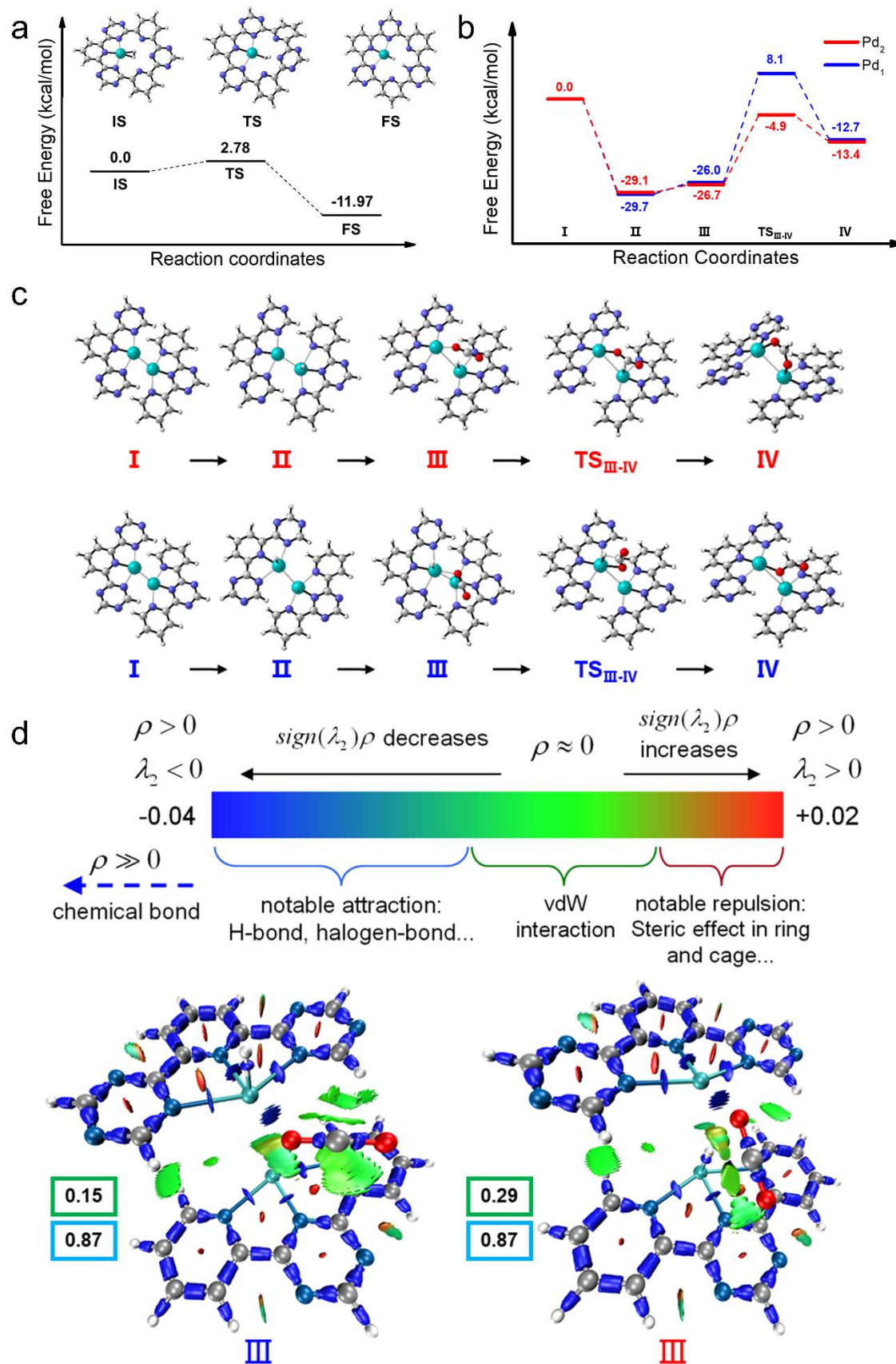


**Fig. 4. DFT calculations.** a, Hydrogen dissociation energy with the structures of the initial state (IS), transition state (TS), and final state (FS). b, Free energy profile of

CO<sub>2</sub> hydrogenation through the Pd<sub>1</sub> pathway and Pd<sub>2</sub> pathway c, Intermediate structures of CO<sub>2</sub> adsorption and hydrogenation in the Pd<sub>1</sub> system and Pd<sub>2</sub> system. d. Isosurface of the interaction region indicator (IRI) for the CO<sub>2</sub> and H co-adsorption configurations in the Pd<sub>1</sub> (left) and Pd<sub>2</sub> (right) system, respectively. The isosurface is mapped according to the function  $IRI = 1.0 \text{ sign}(\lambda_2)\rho$ . The values in the green and blue frames are the atom charges of adsorbed H and C atoms of CO<sub>2</sub>, respectively.

### **Synthesis and catalytic evolution of Pd/[2,6-DCP-CTF] dual single-atom catalyst**

According to the above theoretical model, we calculated the theoretical Pd loadings to be 4.76 wt.% for the ideal dual single-atom catalyst with Pd atom pairs distributed in two close layers. Thus, we tried to prepare Pd/[2,6-DCP-CTF] with abundant dual Pd atoms by increasing the initial Pd loading percentage to 4.0 wt.% and 5.0 wt.%. The actual metal loadings were determined by using inductively coupled plasma atomic emission spectrometry (ICP-AES) to be 3.45 wt.% and 4.40 wt.%, and the corresponding samples were denoted as 3.45Pd/[2,6-DCP-CTF] and 4.4Pd/[2,6-DCP-CTF], respectively. The dispersions of Pd in the above samples were first investigated by TEM at low magnification. As shown in Supplementary Fig. 7a, 3.45Pd/[2,6-DCP-CTF] exhibited the typical morphology of the 2,6-DCP-CTF support without any Pd nanoparticles, which indicated that the Pd species were atomically dispersed. However, Pd nanoparticles appeared in 4.4Pd/[2,6-DCP-CTF] as the Pd loading percentage was close to saturation (Supplementary Fig. 7b). To reveal the fine structure information of Pd in 3.45Pd/[2,6-DCP-CTF], we performed aberration-corrected scanning transmission electron microscopy (AC-STEM) characterization. As shown in Fig. 5a, 3.45Pd/[2,6-DCP-CTF] exhibited abundant white dots, which were identified as Pd species according to the contrast and EDS mapping analysis (Fig. 5b). In the aberration-corrected STEM image at high magnification shown in Fig. 5c, most of the Pd species existed in the form of dual atoms, which were marked with yellow rectangles. In addition, there were few isolated and multiple Pd atoms because of the randomness of the Pd loading process and inhomogeneity of the support. We further quantified the percentage of dual Pd

atoms to be approximately 66% in this range (Fig. 5d). The X-ray absorption near-edge spectroscopy (XANES) and extended X-ray absorption fine structure (EXAFS) were measured to determine the electronic and coordination structures of Pd atoms in  $3.45\text{Pd}/[2,6\text{-DCP-CTF}]$  catalysts. As shown in the Pd K-edge XANES profiles (Fig. 5e), the intensity of the white line of Pd in the  $3.45\text{Pd}/[2,6\text{-DCP-CTF}]$  sample is higher than that of the Pd foil and close to that of PdO, suggesting that the Pd species carry positive charges.<sup>41</sup> XPS was carried out to obtain deeper insight into the electronic properties of  $3.45\text{Pd}/[2,6\text{-DCP-CTF}]$ . (Supplementary Fig. 8) The Pd  $3d_{5/2}$  peak was located at 337.6 eV, indicating a near +2 valence state.<sup>42</sup> The Fourier transform (FT)  $k^3$ -weighted EXAFS spectrum in R space of the  $3.45\text{Pd}/[2,6\text{-DCP-CTF}]$  sample (Fig. 5f) exhibits two obvious peaks. The fitting details are listed in Fig. 5g and Supplementary Table 5. The first prominent peak at 1.75 Å corresponds to the Pd-N coordination path with a coordination number (CN) of  $2.48 \pm 0.88$ . The second peak located at 2.91 Å is attributed to the Pd-Pd coordination path of dual Pd atoms with a CN of  $1.75 \pm 0.624$ . The above parameters are in line with our DFT model (Fig 5 h). Overall, we synthesized Pd/[2,6-DCP-CTF] with abundant dual Pd atoms in the experiment as the theoretical predictions.

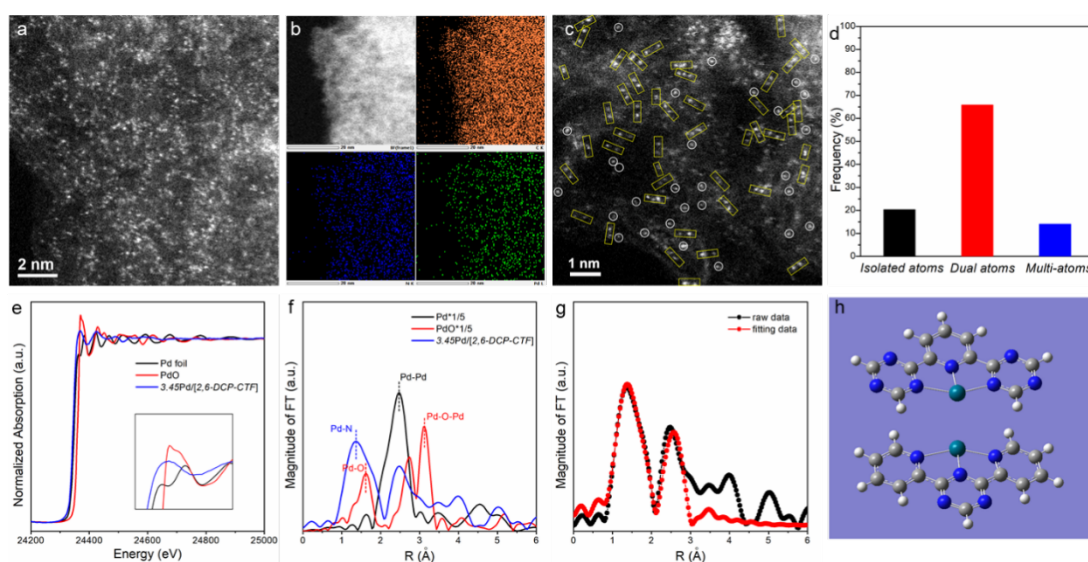


**Fig. 5 Structural and electronic characterizations of Pd/[2,6-DCP-CTF].** a, Aberration-corrected STEM image of the  $3.45\text{Pd}/[2,6\text{-DCP-CTF}]$  catalyst. b, EDS mapping results of  $3.45\text{Pd}/[2,6\text{-DCP-CTF}]$ . c, Aberration-corrected STEM image at

high magnification. d, Histogram of the contents of isolated Pd atoms, dual Pd atoms, and multi-Pd atoms for  $3.45\text{Pd}/[2,6\text{-DCP-CTF}]$ . e, Pd K-edge XANES spectra for  $3.45\text{Pd}/[2,6\text{-DCP-CTF}]$ . Pd foil and PdO were used as the reference. f, Pd K-edge EXAFS in R space for  $3.45\text{Pd}/[2,6\text{-DCP-CTF}]$ . Pd foil and PdO were used as the reference. g, R space fitting curve of  $3.45\text{Pd}/[2,6\text{-DCP-CTF}]$ . h, Structural model of  $\text{Pd}/[2,6\text{-DCP-CTF}]$ .

The  $\text{CO}_2$  sorption properties of the catalysts were investigated using volumetric methods at 273 K and 303 K, and a commercial Pd/C catalyst was used as the reference. As shown in Fig. 6a, b, the  $\text{CO}_2$  adsorption isotherms of both  $3.54\text{Pd}/[2,6\text{-DCP-CTF}]$  and commercial Pd/C displayed reversible adsorption capacity. When the pressure approached 1 bar, the  $\text{CO}_2$  uptake of  $3.54\text{Pd}/[2,6\text{-DCP-CTF}]$  reached 5.05 mmol/g and 2.47 mmol/g at 273 K and 303 K, respectively, which were much higher than those of commercial Pd/C (2.92 mmol/g and 1.49 mmol/g). These results indicate that the rich microporous structure and abundant nitrogen content of  $2,6\text{-DCP-CTF}$  contribute to the enrichment and capture of  $\text{CO}_2$ , which agrees well with the theoretical predictions (Fig. 3c). Furthermore, we compared the  $\text{CO}_2$  adsorption capacities of our  $\text{Pd}/[2,6\text{-DCP-CTF}]$  catalyst with those of excellent  $\text{CO}_2$  capture materials in the literature.<sup>3</sup> As shown in Supplementary Table 6, our catalyst exhibits nearly the highest adsorption capacity under identical conditions. As an excellent  $\text{CO}_2$  capture material with synergistic dual Pd atoms, the  $3.45\text{Pd}/[2,6\text{-DCP-CTF}]$  sample is expected to achieve efficient conversion of carbon dioxide.

The catalytic properties of the as-obtained  $3.45\text{Pd}/[2,6\text{-DCP-CTF}]$  catalyst were evaluated under the same conditions to explore the disparity in catalytic properties between different Pd species, isolated Pd atoms and dual atom pairs. As shown in Fig. 6c, the  $3.45\text{Pd}/[2,6\text{-DCP-CTF}]$  sample was considerably more active than the  $0.82\text{Pd}/[2,6\text{-DCP-CTF}]$  sample, indicating that dual Pd atoms exhibited much higher activity. To demonstrate our assumption, we synthesized a  $\text{Pd}/[2,6\text{-DCP-CTF}]$  sample with a much lower Pd loading (0.39 wt.%), where Pd existed mainly as isolated atoms

(Supplementary Fig. 9). As expected, the  $0.39\text{Pd}/[2,6\text{-DCP-CTF}]$  sample only yielded 0.17 mM formate under ambient conditions (30 °C, 0.1 MPa) after 12 h, and its TOF was measured to be  $0.09\text{ h}^{-1}$ . These results agree well with the theoretical predictions (Fig. 4). In addition, we compared the catalytic activity of our catalysts and a commercial Pd/C catalyst. The results showed that our catalyst exhibited a TOF nearly one order of magnitude higher than that of the commercial Pd/C catalyst. We further investigated the cumulative amount of HCOOH produced within 12 h. As shown in Fig. 6d, upon prolonging the reaction time from 2 h to 4 h, 6 h, 8 h, 10 h and 12 h, the yield of formate increased linearly from 0.14 mmol to 0.26 mmol, 0.37 mmol, 0.47 mmol, 0.56 mmol, and 0.68 mmol, and the TON of the most active catalyst reached 103.68. This indicates that product accumulation has little influence on the reaction and that the catalyst exhibits good stability during the reaction process. Furthermore, we optimized the activity of our catalysts by screening the additives. As shown in Supplementary Table 7,  $3.45\text{Pd}/[2,6\text{-DCP-CTF}]$  exhibited much higher activity with 1 M  $\text{Na}_2\text{CO}_3$  as the additive, and the TOFs reached  $13.46\text{ h}^{-1}$  under ambient conditions (30 °C, 1 bar). In addition, we also investigated the direct hydrogenation of  $\text{Na}_2\text{CO}_3$  and found that formate production was negligible without gaseous  $\text{CO}_2$  in the reactant.

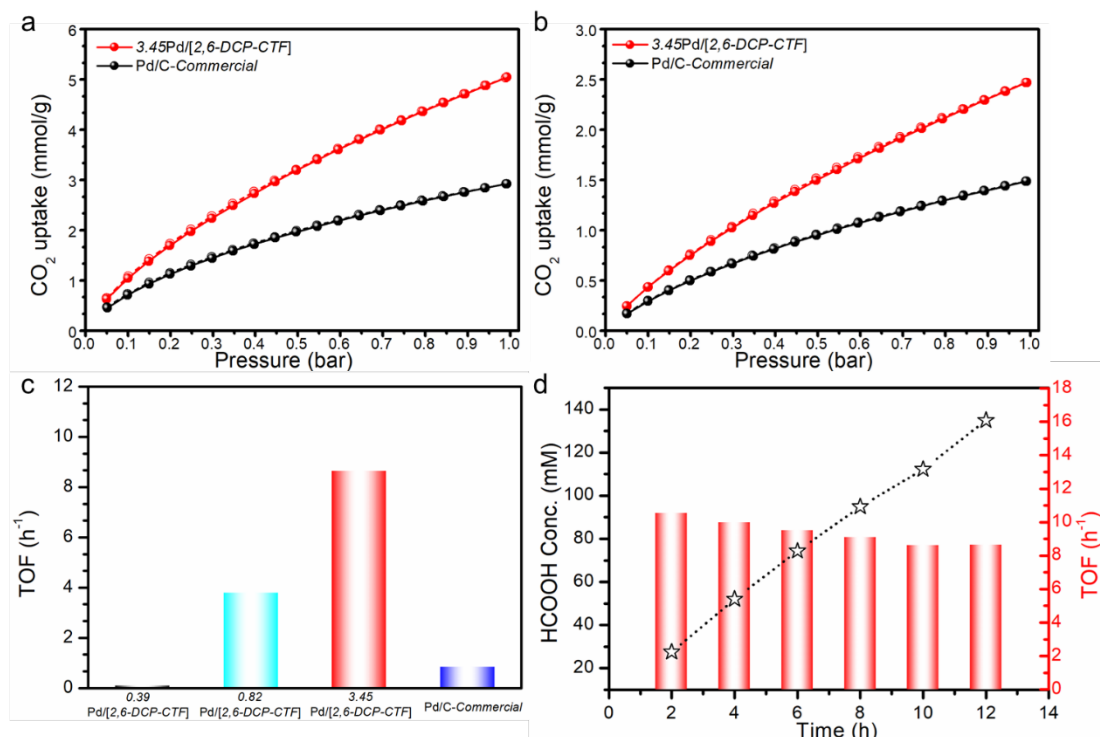


**Fig. 6 Catalyst performance and CO<sub>2</sub> uptake data.** a, b, CO<sub>2</sub> adsorption (solid symbols) and desorption (open symbols) isotherms of 3.45Pd/[2,6-DCP-CTF] and commercial Pd/C. c, TOF for the hydrogenation of CO<sub>2</sub> into formate over different catalysts. d, Formate yield during the hydrogenation of CO<sub>2</sub> over 3.45Pd/[2,6-DCP-CTF]. Reaction conditions: 20 mg catalyst, 30 °C, 1 bar (CO<sub>2</sub>/H<sub>2</sub>=1:1), 5 mL NaHCO<sub>3</sub> (1 M), 12 h.

## Conclusion

In summary, we have realized effective hydrogenation of CO<sub>2</sub> to formate under ambient conditions on heterogeneous catalysts for the first time. Theoretical calculations based on the DFT method predicted the most active structure of the catalyst to be the ternary synergistic sites in the microporous material (2,6-DCP-CTF) with pore enrichment effect for CO<sub>2</sub>. In details, Pd-N synergistic site is favorable for hydrogen dissociation, and Pd-Pd synergistic site for high efficient CO<sub>2</sub> hydrogenation. In experiments, we prepared Pd/[2,6-DCP-CTF] SACs with abundant dual Pd atom pairs derived from different layers of 2,6-DCP-CTF by

regulating the Pd loading percentage and demonstrated that synergistic dual Pd atoms on *2,6-DCP-CTF* can capture a significant amount of CO<sub>2</sub> (5.05 mmol/g, 273 K) and efficiently convert CO<sub>2</sub> to formic acid under ambient conditions with a turnover frequency (TOF) as high as 13.46 h<sup>-1</sup>. This work provides an effective strategy to generate excellent catalysts with high catalytic activity and may pave the way for converting CO<sub>2</sub> to many more liquid fuels under ambient conditions.

## Methods

### Sample preparation

*2,6-DCP-CTF*: *2,6*-Pyridinedicarbonitrile-derived covalent triazine framework (*2,6-DCP-CTF*) samples were synthesized by the traditional ionothermal method. Specifically, *2,6-DCP* (3 g) and anhydrous ZnCl<sub>2</sub> (15 g) were mixed in a glove box and then transferred into a Pyrex ampule under an inert atmosphere. The ampule was evacuated with a vacuum pump, sealed, and heated to 400 °C for 20 h and then 600 °C for 20 h. The ampule was then cooled to room temperature and opened carefully. The reaction mixture was subsequently ground and then washed thoroughly with large amounts of water to remove most of the ZnCl<sub>2</sub>. Further stirring in diluted HCl (2 M) for 12 h was carried out to remove the residual salt. After this purification step, the resulting black powder was filtered, washed successively with water, and dried in vacuum at 150 °C for 12 h.

*M/[2,6-DCP-CTF]*: *M/[2,6-DCP-CTF]* catalysts (M = Ru, Rh, Pd, Ir, Pt, Au) were prepared by soaking *2,6-DCP-CTF* support powder in aqueous solutions with 1 wt.% theoretical metal weight loadings of ruthenium chloride, rhodium chloride, palladium trifluoroacetate, chloroiridic acid, chloroplatinic acid and chloroauric acid (Shanghai Macklin Biochemical Co., Ltd) for 12 h with magnetic stirring under N<sub>2</sub> atmosphere. The suspensions were then filtered and washed with deionized water. The filter cake was dried at 80 °C for 12 h under vacuum. The samples were denoted as *M/[2,6-DCP-CTF]* (M = Ru, Rh, Pd, Ir, Pt, Au). Pd/[*2,6-DCP-CTF*] SACs with different Pd atom densities were prepared by varying the initial Pd loading percent.

The actual metal weight loadings were detected using inductively coupled plasma atomic emission spectrometry (ICP-AES) analysis.

### **Characterization**

The actual loadings of the noble metals were determined by using ICP-AES on an IRIS intrepid II XSP instrument (Thermo Electron Corporation).

Fourier transform infrared (FT-IR) spectra were collected on a Bruker VERTEX 70v spectrometer equipped with a DLATGS detector using KBr pellets and operated at a resolution of  $4\text{ cm}^{-1}$  for 32 scans.

Specific Surface areas were measured on a Quantachrome Autosorb-iQ using  $\text{N}_2$  adsorption isotherms and the Brunauer-Emmett-Teller (BET) analysis method. The samples were degassed under vacuum at  $260\text{ }^\circ\text{C}$  for 8 h before the adsorption measurements.

$\text{CO}_2$  adsorption isotherms were measured on a Quantachrome Autosorb-iQ using  $\text{CO}_2$  as the adsorbate. The samples were degassed under vacuum at  $260\text{ }^\circ\text{C}$  for 8 h before the adsorption measurements.

X-ray photoelectron spectroscopy (XPS) data were collected using a ThermoFisher ESCALAB 250Xi spectrometer with a monochromatized Al  $\text{K}\alpha$  X-ray source ( $1486.6\text{ eV}$ ) and an applied power of 150 W.  $\text{C}_{1s}$  (binding energy  $284.8\text{ eV}$ ) was used as the reference.

The X-ray absorption spectra (XAS) including X-ray absorption near-edge structure (XANES) and extended X-ray absorption fine structure (EXAFS) of the sample at K-edge was collected at the Beamline of TPS44A1 in National Synchrotron Radiation Research Center (NSRRC), Taiwan. A pair of channel-cut Si (111) crystals was used in the monochromator. The spectra were recorded at room temperature under the fluorescence mode with a solid-state detector. The Athena software package was used for the data analysis.

Transmission electron microscopy (TEM) analysis was performed by using a FEI

Tecnai G2 F20 operated at 200 keV with a specified point-to-point resolution of 0.27 nm. Aberration-corrected high angle annular dark field scanning transmission electron microscopy (AC-HAADF-STEM) and energy dispersive X-ray spectroscopy (EDX) images were obtained on a JEOL JEM-ARM200F STEM/TEM system with a guaranteed resolution of 0.08 nm. TEM specimens were prepared by depositing a suspension of the powdered sample on lacey carbon-coated copper grids.

### **Catalytic reactions**

CO<sub>2</sub> hydrogenation to formic acid was performed at 30 °C and 1 bar (H<sub>2</sub>:CO<sub>2</sub> = 1:1). In a typical hydrogenation experiment, 20 mg catalyst and 5 mL NaHCO<sub>3</sub> (1 M) were added to a three-necked bottle connected to a balloon. Then, the feed gas was introduced after purging the residual air in the system three times, and the reaction mixture was stirred at 30 °C for 12 h. Formic acid concentrations were determined using high-performance liquid chromatography (HPLC) with an Agilent 1260 II instrument and a Hi-Plex H column and UV detector (210 nm) using 0.005 M H<sub>2</sub>SO<sub>4</sub> as the mobile phase.

### **Computational methods**

The first hydrogenation step of CO<sub>2</sub> to formate was calculated using the program Gaussian16 for preliminary screening.<sup>43</sup> Calculations were performed by the M06l/6-31G\* method for nonmetal elements and the M06l/LANL2DZ method for metal atoms.<sup>44, 45, 46</sup> The metals were augmented with the corresponding LANL2DZ pseudopotential, which is acceptable in terms of both precision and time requirements. The SMD solvation model<sup>47</sup> was applied for the simulation in dual Pd systems. The vibrational frequencies of the optimized configurations were analysed to validate that these configurations correspond to a local minimum or transition state (TS). A TS with one imaginary frequency was found and verified by the intrinsic reaction coordinate (IRC) method.<sup>48</sup>

The periodic structure was optimized using the classical molecular mechanical method using a universal force field<sup>49</sup>. The grand canonical Monte Carlo (GCMC )

method and COMPASS force field<sup>50</sup> were used to predict the CO<sub>2</sub> uptake performance. In every GCMC simulation, 1,000,000 equilibration steps were used before the production stage of 3,000,000 Monte Carlo steps.

The calculation method was based on metal ions with a valence state of 2 or higher that are stably anchored on 2,6-DCP-CTF. 2,6-DCP-CTF has a periodic two-dimensional microporous structure. To reduce the computational complexity, part of 2,6-DCP-CTF was constructed as a catalytic unit, named 2,6-DCP-CTF-[M] ([M] = Ru<sup>3+</sup>, Rh<sup>3+</sup>, Pd<sup>2+</sup>, Ir<sup>3+</sup>, Pt<sup>2+</sup>, Au<sup>3+</sup>, Os<sup>4+</sup>).

## Data availability

The data that support the findings of this study are available from the authors upon reasonable request.

## Reference

1. Aresta M, Dibenedetto A, Angelini A. Catalysis for the Valorization of Exhaust Carbon: from CO<sub>2</sub> to Chemicals, Materials, and Fuels. Technological Use of CO<sub>2</sub>. *Chem Rev* 2014, **114**(3): 1709-1742.
2. Senftle TP, Carter EA. The Holy Grail: Chemistry Enabling an Economically Viable CO<sub>2</sub> Capture, Utilization, and Storage Strategy. *Acc Chem Res* 2017, **50**(3): 472-475.
3. Dawson R, Stockel E, Holst JR, Adams DJ, Cooper AI. Microporous organic polymers for carbon dioxide capture. *Energ Environ Sci* 2011, **4**(10): 4239-4245.
4. Alvarez A, Bansode A, Urakawa A, Bavykina AV, Wezendonk TA, Makkee M, *et al.* Challenges in the Greener Production of Formates/Formic Acid, Methanol, and DME by Heterogeneously Catalyzed CO<sub>2</sub> Hydrogenation Processes. *Chem Rev* 2017, **117**(14): 9804-9838.
5. Su X, Yang XF, Huang YQ, Liu B, Zhang T. Single-Atom Catalysis toward Efficient CO<sub>2</sub> Conversion to CO and Formate Products. *Acc Chem Res* 2019, **52**(3): 656-664.
6. Eppinger J, Huang KW. Formic Acid as a Hydrogen Energy Carrier. *Acs Energy Lett* 2017, **2**(1): 188-195.
7. Xia C, Zhu P, Jiang Q, Pan Y, Liang WT, Stavitsk E, *et al.* Continuous production of pure liquid fuel solutions via electrocatalytic CO<sub>2</sub> reduction using solid-electrolyte devices. *Nat Energy* 2019, **4**(9): 776-785.
8. Tian ZB, Dong C, Yu Q, Ye RP, Duyar MS, Liu J, *et al.* A universal nanoreactor strategy for scalable supported ultrafine bimetallic nanoparticles synthesis. *Mater Today* 2020, **40**: 72-81.
9. Filonenko GA, van Putten R, Schulpen EN, Hensen EJM, Pidko EA. Highly Efficient Reversible Hydrogenation of Carbon Dioxide to Formates Using a Ruthenium PNP-Pincer Catalyst. *ChemCatChem* 2014, **6**(6): 1526-1530.

10. Inoue Y, Izumida H, Sasaki Y, Hashimoto H. Catalytic Fixation of Carbon-Dioxide to Formic-Acid by Transition-Metal Complexes under Mild Conditions. *Chem Lett* 1976(8): 863-864.
11. Tanaka R, Yamashita M, Nozaki K. Catalytic Hydrogenation of Carbon Dioxide Using Ir(III)-Pincer Complexes. *J Am Chem Soc* 2009, **131**(40): 14168-14169.
12. Gunasekar GH, Shin J, Jung KD, Park K, Yoon S. Design Strategy toward Recyclable and Highly Efficient Heterogeneous Catalysts for the Hydrogenation of CO<sub>2</sub> to Formate. *ACS Catal* 2018, **8**(5): 4346-4353.
13. Zhang YP, Fei JH, Yu YM, Zheng XM. Silica immobilized ruthenium catalyst used for carbon dioxide hydrogenation to formic acid (I): the effect of functionalizing group and additive on the catalyst performance. *Catal Commun* 2004, **5**(10): 643-646.
14. Liu Q, Yang X, Li L, Miao S, Li Y, Li Y, *et al.* Direct catalytic hydrogenation of CO<sub>2</sub> to formate over a Schiff-base-mediated gold nanocatalyst. *Nat Commun* 2017, **8**(1): 1407.
15. Shao X, Yang X, Xu J, Liu S, Miao S, Liu X, *et al.* Iridium Single-Atom Catalyst Performing a Quasi-homogeneous Hydrogenation Transformation of CO<sub>2</sub> to Formate. *Chem* 2019, **5**: 693-705.
16. Filonenko GA, Vrijburg WL, Hensen EJM, Pidko EA. On the activity of supported Au catalysts in the liquid phase hydrogenation of CO<sub>2</sub> to formates. *J Catal* 2016, **343**: 97-105.
17. Himeda Y, Onozawa-Komatsuzaki N, Sugihara H, Kasuga K. Simultaneous tuning of activity and water solubility of complex catalysts by acid-base equilibrium of ligands for conversion of carbon dioxide. *Organometallics* 2007, **26**(3): 702-712.
18. Wang WH, Hull JF, Muckerman JT, Fujita E, Himeda Y. Second-coordination-sphere and electronic effects enhance iridium(III)-catalyzed homogeneous hydrogenation of carbon dioxide in water near ambient temperature and pressure. *Energ Environ Sci* 2012, **5**(7): 7923-7926.
19. Hull JF, Himeda Y, Wang WH, Hashiguchi B, Periana R, Szalda DJ, *et al.* Reversible hydrogen storage using CO<sub>2</sub> and a proton-switchable iridium catalyst in aqueous media under mild temperatures and pressures. *Nat Chem* 2012, **4**(5): 383-388.
20. Wang WH, Muckerman JT, Fujita E, Himeda Y. Mechanistic Insight through Factors Controlling Effective Hydrogenation of CO<sub>2</sub> Catalyzed by Bioinspired Proton-Responsive Iridium(III) Complexes. *ACS Catal* 2013, **3**(5): 856-860.
21. Kanega R, Onishi N, Szalda DJ, Ertem MZ, Muckerman JT, Fujita E, *et al.* CO<sub>2</sub> Hydrogenation Catalysts with Deprotonated Picolinamide Ligands. *ACS Catal* 2017, **7**(10): 6426-6429.
22. Jeletic MS, Mock MT, Appel AM, Linehan JC. A Cobalt-Based Catalyst for the Hydrogenation of CO<sub>2</sub> under Ambient Conditions. *J Am Chem Soc* 2013, **135**(31): 11533-11536.
23. Lang R, Li TB, Matsumura D, Miao S, Ren YJ, Cui YT, *et al.* Hydroformylation of Olefins by a Rhodium Single-Atom Catalyst with Activity Comparable to RhCl(PPh<sub>3</sub>)<sub>3</sub>. *Angew Chem, Int Ed* 2016, **55**(52): 16054-16058.
24. Qiao BT, Wang AQ, Yang XF, Allard LF, Jiang Z, Cui YT, *et al.* Single-atom catalysis of CO oxidation using Pt-1/FeOx. *Nat Chem* 2011, **3**(8): 634-641.
25. Yang XF, Wang AQ, Qiao BT, Li J, Liu JY, Zhang T. Single-Atom Catalysts: A New Frontier in Heterogeneous Catalysis. *Acc Chem Res* 2013, **46**(8): 1740-1748.

26. Wang AQ, Li J, Zhang T. Heterogeneous single-atom catalysis. *Nat Rev Chem* 2018, **2**(6): 65-81.
27. Shao XZ, Yang XF, Xu JM, Liu S, Miao S, Liu XY, *et al.* Iridium Single-Atom Catalyst Performing a Quasi-homogeneous Hydrogenation Transformation of CO<sub>2</sub> to Formate. *Chem* 2019, **5**(3): 693-705.
28. Ge Y, Qin X, Li A, Deng Y, Lin L, Zhang M, *et al.* Maximizing the Synergistic Effect of CoNi Catalyst on  $\alpha$ -MoC for Robust Hydrogen Production. *J Am Chem Soc* 2020, **143**(2): 628-633.
29. Wang J, You R, Zhao C, Zhang W, Liu W, Fu X-P, *et al.* N-Coordinated Dual-Metal Single-Site Catalyst for Low-Temperature CO Oxidation. *ACS Catal* 2020, **10**(4): 2754-2761.
30. Yang Y, Qian YM, Li HJ, Zhang ZH, Mu YW, Do D, *et al.* O-coordinated W-Mo dual-atom catalyst for pH-universal electrocatalytic hydrogen evolution. *Sci Adv* 2020, **6**(23): eaba6586.
31. Li HL, Wang LB, Dai YZ, Pu ZT, Lao ZH, Chen YW, *et al.* Synergetic interaction between neighbouring platinum monomers in CO<sub>2</sub> hydrogenation. *Nat Nanotechnol* 2018, **13**(5): 411-417.
32. Guan AX, Chen Z, Quan YL, Peng C, Wang ZQ, Sham SK, *et al.* Boosting CO<sub>2</sub> Electroreduction to CH<sub>4</sub> via Tuning Neighboring Single-Copper Sites. *Acs Energy Lett* 2020, **5**(4): 1044-1053.
33. Li YF, Chen C, Cao R, Pan ZW, He H, Zhou KB. Dual-atom Ag<sub>2</sub>/graphene catalyst for efficient electroreduction of CO<sub>2</sub> to CO. *Appl Catal B-Environ* 2020, **268**: 118747.
34. Ouyang YX, Shi SL, Bai XW, Li Q, Wang JL. Breaking scaling relations for efficient CO<sub>2</sub> electrochemical reduction through dual-atom catalysts. *Chem Sci* 2020, **11**(7): 1807-1813.
35. Liu Q, Yang XF, Li L, Miao S, Li Y, Li YQ, *et al.* Direct catalytic hydrogenation of CO<sub>2</sub> to formate over a Schiff-base-mediated gold nanocatalyst. *Nat Commun* 2017, **8**: 1407.
36. Li YJ, Zheng SH, Liu X, Li P, Sun L, Yang RX, *et al.* Conductive Microporous Covalent Triazine-Based Framework for High-Performance Electrochemical Capacitive Energy Storage. *Angew Chem, Int Ed* 2018, **57**(27): 7992-7996.
37. Xie Y, Wang TT, Liu XH, Zou K, Deng WQ. Capture and conversion of CO<sub>2</sub> at ambient conditions by a conjugated microporous polymer. *Nat Commun* 2013, **4**.
38. Zhou W, Deng QW, Ren GQ, Sun L, Yang L, Li YM, *et al.* Enhanced carbon dioxide conversion at ambient conditions via a pore enrichment effect. *Nat Commun* 2020, **11**(1).
39. Lu T, Chen FW. Multiwfn: A multifunctional wavefunction analyzer. *J Comput Chem* 2012, **33**(5): 580-592.
40. Lu T, Chen Q. Interaction Region Indicator: A Simple Real Space Function Clearly Revealing Both Chemical Bonds and Weak Interactions. *Chemistry-Methods* 2021, **1**(5): 231-239.
41. Liu J, Chen ZX, Liu CB, Zhang B, Du YH, Liu CF, *et al.* Molecular engineered palladium single atom catalysts with an M-C<sub>1</sub>N<sub>3</sub> subunit for Suzuki coupling. *J Mater Chem A* 2021.
42. Huang XH, Yan H, Huang L, Zhang XH, Lin Y, Li JJ, *et al.* Toward Understanding of the Support Effect on Pd-1 Single-Atom-Catalyzed Hydrogenation Reactions. *J Phys Chem C* 2019, **123**(13): 7922-7930.
43. Humphrey W, Dalke A, Schulten K. VMD: Visual molecular dynamics. *J Mol Graph Model* 1996, **14**(1): 33-38.
44. Hay PJ, Wadt WR. Abinitio Effective Core Potentials for Molecular Calculations - Potentials for K to Au Including the Outermost Core Orbitals. *J Chem Phys* 1985, **82**(1): 299-310.
45. Hehre WJ, Ditchfield R, Pople JA. Self-Consistent Molecular-Orbital Methods .12. Further

- Extensions of Gaussian-Type Basis Sets for Use in Molecular-Orbital Studies of Organic-Molecules. *J Chem Phys* 1972, **56**(5): 2257-2261.
46. Zhao Y, Truhlar DG. A new local density functional for main-group thermochemistry, transition metal bonding, thermochemical kinetics, and noncovalent interactions. *J Chem Phys* 2006, **125**(19): 194101.
47. Marenich AV, Cramer CJ, Truhlar DG. Universal Solvation Model Based on Solute Electron Density and on a Continuum Model of the Solvent Defined by the Bulk Dielectric Constant and Atomic Surface Tensions. *J Phys Chem B* 2009, **113**(18): 6378-6396.
48. Fukui K. The Path of Chemical-Reactions - the Irc Approach. *Acc Chem Res* 1981, **14**(12): 363-368.
49. Rappe AK, Casewit CJ, Colwell KS, Goddard WA, Skiff WM. Uff, a Full Periodic-Table Force-Field for Molecular Mechanics and Molecular-Dynamics Simulations. *J Am Chem Soc* 1992, **114**(25): 10024-10035.
50. Sun H. COMPASS: An ab initio force-field optimized for condensed-phase applications - Overview with details on alkane and benzene compounds. *J Phys Chem B* 1998, **102**(38): 7338-7364.

## Acknowledgment

This work was supported by the National Key Research and Development Program of China (No. 2017YFA0204800), the National Natural Science Foundation of China (No. 21525315), Natural Science Foundation of Shandong Province (ZR2020QB056), and the Fundamental Research Funds of Shandong University (2019GN021 to G.Q.R, 2019GN111 to T. Y. and 2019HW016 to L.S.).

## Author Contributions

W. -Q. D. conceived the concept and design research. G.- Q. R. designed and carried out the catalyst synthesis, characterization, and catalytic test. S.-L. Z. carried out the catalyst synthesis, characterization, and catalytic test. L. S., J.-K. S. and L. Y. executed the theoretical calculations. T. Y. carried out the TEM characterization. All authors were involved in the writing of the manuscript.

## Competing interests

The authors declare no competing interests.